



Fast Radio Bursts' Recipes for the Distributions of Dispersion Measures, Flux Densities, and Fluences

Yuu Niino 

National Astronomical Observatory of Japan, 2-21-1 Osawa, Mitaka, Tokyo, Japan; yuuniino@nao.ac.jp
 Received 2018 January 19; revised 2018 March 9; accepted 2018 March 22; published 2018 April 26

Abstract

We investigate how the statistical properties of dispersion measure (DM) and apparent flux density/fluence of (nonrepeating) fast radio bursts (FRBs) are determined by unknown cosmic rate density history [$\rho_{\text{FRB}}(z)$] and luminosity function (LF) of the transient events. We predict the distributions of DMs, flux densities, and fluences of FRBs taking account of the variation of the receiver efficiency within its beam, using analytical models of $\rho_{\text{FRB}}(z)$ and LF. Comparing the predictions with the observations, we show that the cumulative distribution of apparent fluences suggests that FRBs originate at cosmological distances and ρ_{FRB} increases with redshift resembling the cosmic star formation history (CSFH). We also show that an LF model with a bright-end cutoff at $\log_{10} L_{\nu}$ ($\text{erg s}^{-1} \text{Hz}^{-1}$) ~ 34 are favored to reproduce the observed DM distribution if $\rho_{\text{FRB}}(z) \propto \text{CSFH}$, although the statistical significance of the constraints obtained with the current size of the observed sample is not high. Finally, we find that the correlation between DM and flux density of FRBs is potentially a powerful tool to distinguish whether FRBs are at cosmological distances or in the local universe more robustly with future observations.

Key words: intergalactic medium – ISM: general – radio continuum: general

1. Introduction

Fast radio bursts (FRBs) are transient events observed in ~ 1 GHz radio bands with typical durations of several milliseconds (e.g., Lorimer et al. 2007; Keane et al. 2012; Thornton et al. 2013). Their large dispersion measures (DMs), which indicate the column density of free electrons along the sightlines, suggest that they are extragalactic objects. If FRB DMs arise from the intergalactic medium (IGM), FRBs may provide us with an unprecedented opportunity to detect the IGM directly.

However, the origin of FRBs is not yet known. Although various theoretical models have been proposed (e.g., Kashiyama et al. 2013; Popov & Postnov 2013; Totani 2013; Falcke & Rezzolla 2014; Cordes & Wasserman 2016; Zhang 2017), observational evidence that confirms or rejects those models is hardly obtained. The currently available localization precision of FRBs is typically several arcmin, which is too large to identify their host galaxies, and FRB distance measurements that are independent of DM are also missing.

The only exception is FRB 121102, the repeating FRB, for which the host galaxy is identified and its redshift is known thanks to its repeatability (Chatterjee et al. 2017; Tendulkar et al. 2017). However, the other FRBs do not show any repeatability, and hence FRB 121102 can be a different kind of phenomenon from the other FRBs (Palaniswamy & Zhang 2018), although it is also pointed out that FRB 110220 and FRB 140514 might be repetitions of a same source (Piro & Burke-Spolaor 2017). Hereafter, FRB means nonrepeating FRB, unless stated otherwise.

Redshift distribution of a population of transient events is an important clue to understand the nature of the transients, which reflects their luminosity function (LF) and comoving rate density at each redshift. The cosmic FRB rate density [$\rho_{\text{FRB}}(z)$] would be proportional to the cosmic star formation history (CSFH) if FRBs are related to the young stellar population

(e.g., core-collapse supernovae, young neutron stars), while it would follow the cosmic stellar mass density (CSMD) if FRBs arise from older stars.

Although we cannot measure redshift of an FRB in most cases, distance to an FRB can be estimated via its DM. The excess of the DM over the Milky Way contribution in the direction (DM_{EX}) can be interpreted as the distance to the source under the assumption that a major part of the observed DM_{EX} arises from the IGM (e.g., Ioka 2003; Inoue 2004). Previous studies have shown that the DM_{EX} distribution of the observed FRBs is consistent with the expectations if FRBs are distributed over cosmological distance (e.g., Dolag et al. 2015; Caleb et al. 2016; Katz 2016; Cao et al. 2017). However, DM_{EX} does not necessarily arise only from the IGM, because a part of DM_{EX} can be attributed to ionized gas in the vicinity of FRBs.

The cumulative distribution of FRB flux densities/fluences (so-called $\log N$ – $\log S$ distribution) also serves as a clue to understand the distance distribution of FRBs, because the distribution follows a power law with the index of -1.5 when the sources are uniformly distributed in a Euclidean space, while the distribution may vary when the sources are at cosmological distances due to the cosmic expansion and cosmological evolution of the source number density (Caleb et al. 2016; Katz 2016; Oppermann et al. 2016; Vedantham et al. 2016; Li et al. 2017; Macquart & Ekers 2018).

In this study, we investigate how the interplay between unknown cosmic rate density history and LF of FRBs determines the statistical properties of the observable quantities, i.e., DM_{EX} and apparent flux density/fluence, taking account of the variation of the receiver efficiency within its beam. We discuss what constraint the current observations put on the nature of FRBs and how we can distinguish whether FRBs are at cosmological distances or in the local universe with future observations.

In Sections 2 and 3, we describe our models of cosmic FRB rate history and FRB LF, respectively. We discuss constraints

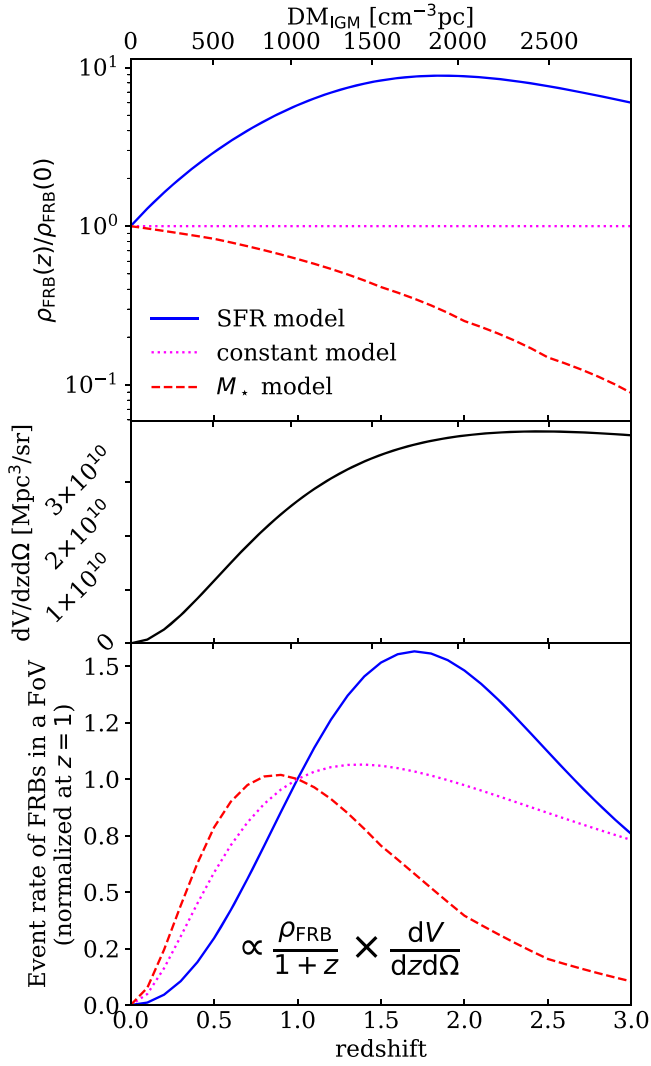


Figure 1. Top panel: ρ_{FRB} models (occurrence rate of FRBs per comoving volume) normalized at $z = 0$. Middle panel: observed comoving volume per redshift per steradian with the assumed cosmology ($dV/dz d\Omega$). Bottom panel: occurrence rate of FRBs per redshift per steradian in the observer frame, which is proportional to $\rho_{\text{FRB}}(z)/(1+z) \times dV/dz d\Omega$. We note that the FRB rates shown in this figure represent all FRBs regardless of their detectability. The DM_{IGM} that corresponds to each redshift is indicated in the upper horizontal axis (see Equation (2)).

on the cosmic rate history and the LF of FRBs obtained from the observed DM_{EX} distribution under the assumption that FRBs originate at cosmological distances in Section 4. In Section 5, we discuss the $\log N$ – $\log S$ distribution and the correlation between DM_{EX} and apparent flux density of FRBs, comparing the predictions of the cosmological and local FRB models. In Section 6, we discuss a couple of uncertainties that may potentially affect our results. Our conclusions are summarized in Section 7. Throughout this paper, we assume the fiducial cosmology with $\Omega_{\Lambda} = 0.7$, $\Omega_m = 0.3$, and $H_0 = 70 \text{ km s}^{-1} \text{ Mpc}^{-1}$.

2. Cosmic FRB Rate History and DM_{IGM} Distribution

We consider three models of ρ_{FRB} in this study (the top panel of Figure 1). One is proportional to CSFH (SFR model), another is constant throughout cosmic time (constant model), and the other is proportional to CSMD (M_* model). We use the

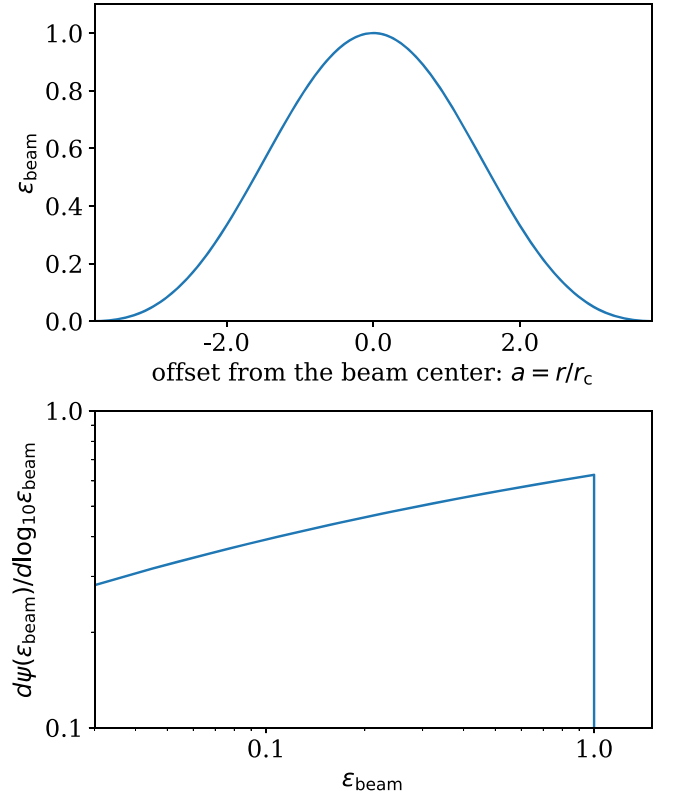


Figure 2. Top panel: the Airy disk model of a radio receiver beam efficiency as a function of the offset from the beam center. Bottom panel: the efficiency PDF within an Airy disk beam.

formulations of CSFH and CSMD by Madau & Dickinson (2014).

The redshift distribution of FRBs that occur in a unit area on the sky within a certain time period in the observer frame can be expressed as

$$\frac{dN(z)}{dz d\Omega} = \frac{\rho_{\text{FRB}}(z)}{1+z} \times \frac{dV}{dz d\Omega}, \quad (1)$$

where $dV/dz d\Omega$ is comoving volume per redshift per observed area (the middle panel of Figure 1).

DM that arise from the IGM can be expressed as

$$\text{DM}_{\text{IGM}} = c \int_0^z \left| \frac{dt}{dz'} \right| \frac{n_{e,\text{IGM}}(z')}{1+z'} dz', \quad (2)$$

where $n_{e,\text{IGM}}$ is the electron density in the IGM. Here we assume that the IGM is uniform at each redshift with the comoving density $\rho_{\text{crit}} \Omega_b$, composed of 75% H and 25% He, and fully ionized throughout the redshift range we consider. Under these assumptions, the IGM electron density can be written as

$$n_{e,\text{IGM}}(z) = \frac{7}{8} \frac{\rho_{\text{crit}} \Omega_b}{m_p} (1+z)^3. \quad (3)$$

The upper horizontal axis of Figure 1 indicates DM_{IGM} that corresponds to z in the lower axis (naively, $\text{DM}_{\text{IGM}} \sim 1000z \text{ cm}^{-3} \text{ pc}$ in this redshift range).

In the above expression, it is assumed that the dominant fraction of baryons in the universe is in the IGM, which is true when we consider diffuse ionized gas associated with dark matter halos as part of the IGM (e.g., Fukugita & Peebles 2004).

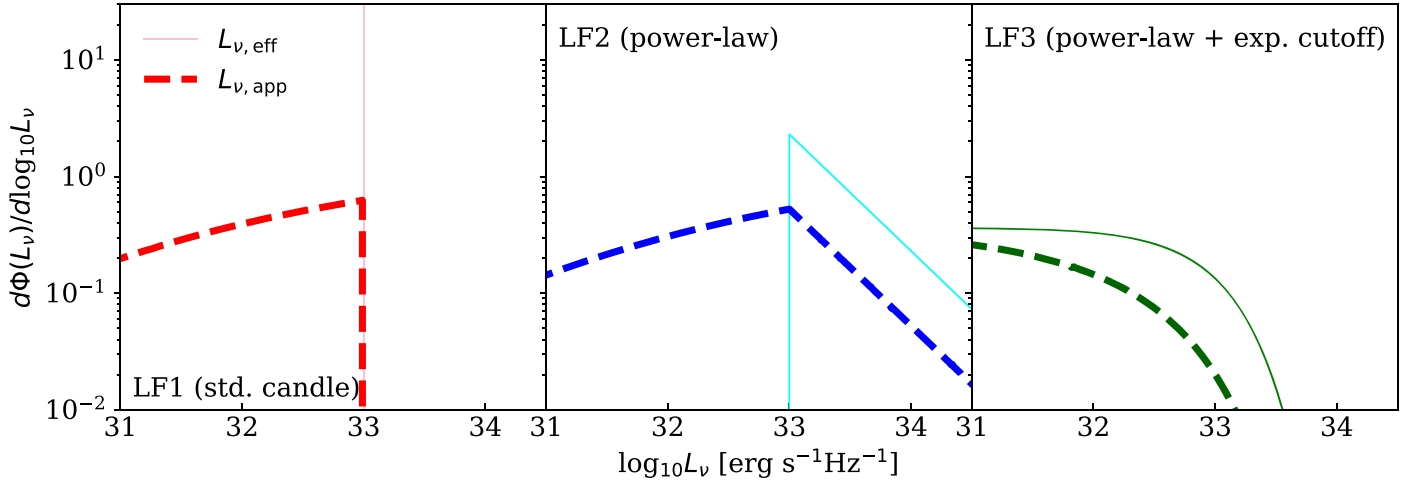


Figure 3. FRB luminosity function models considered in this study. The left, middle, and right panels show the PDFs of $L_{\nu,\text{eff}}$ (thin solid) and $L_{\nu,\text{app}}$ (thick dashed) for LF1 (standard candles), LF2 (power-law), and LF3 (power-law + exponential cutoff), respectively. The PDFs with $\log_{10} L_{\nu,0}$ ($\text{erg s}^{-1} \text{Hz}^{-1}$) = 33 are shown for each model.

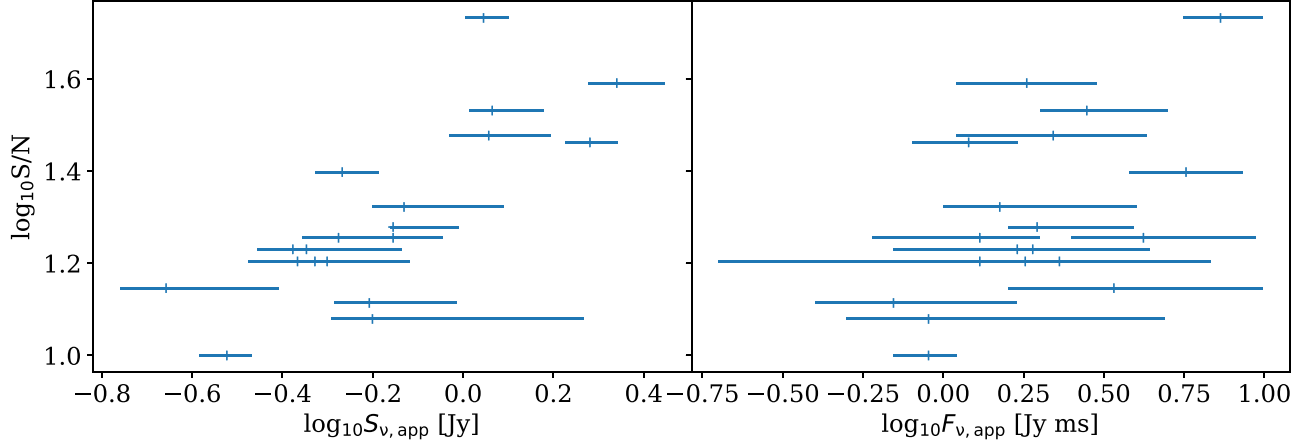


Figure 4. Left panel: the correlation between $S_{\nu,\text{app}}$ and S/N in the Parkes sample. Right panel: same as the left panel but between $F_{\nu,\text{app}}$ and S/N . The two peculiarly bright events, FRB 010724 and 150807, are excluded.

If a significant part of the IGM is associated with dark matter halos, the IGM might be inhomogeneous in reality, and the inhomogeneity might affect the DM_{IGM} distribution of FRBs. We discuss the effect of the IGM inhomogeneity on our results in Section 6.1

The predicted redshift distributions with the three $\rho_{\text{FRB}}(z)$ models are shown in the bottom panel of Figure 1. The redshift distributions with the different $\rho_{\text{FRB}}(z)$ models are similar to each other at $z \lesssim 1$, where the majority of the currently known FRBs reside, while the redshift distributions are dramatically different at $z > 1$, as previously shown by Dolag et al. (2015) using cosmological simulations. We note that detectability of FRB events are not considered here and the redshift distributions may include FRBs that are too faint to be detected. We discuss a fraction of detectable FRBs at each redshift in Section 3.

3. FRB Luminosity and Receiver Efficiency

3.1. Receiver Efficiency Variation within a Beam

The observed radio flux density of an FRB at the peak of its light curve ($S_{\nu,\text{app}}$) does not depend solely on its luminosity and distance; it also depends on the unknown position of the FRB within the receiver beam, because the efficiency of a radio

receiver largely varies within its beam. We assume that a beam efficiency pattern of a radio receiver under consideration is represented by an Airy disk

$$\epsilon_{\text{beam}}(a) = \left[\frac{2J_1(a)}{a} \right]^2, \quad (4)$$

where the efficiency at the beam center is unity, J_1 is the first-order Bessel function of the first kind, and $a = r/r_c$ is the offset from the beam center normalized by the beam characteristic radius (the top panel of Figure 2). The efficiency is 50% at $a = 1.62$ and drops to zero at $a = 3.83$ ($\equiv a_{\text{out}}$). For the Parkes multibeam receiver (Staveley-Smith et al. 1996), whose full width at half maximum (FWHM) is 14.4 arcmin, r_c is 4.4 arcmin. We do not consider sidelobe detections ($|a| > a_{\text{out}}$).

The probability distribution function (PDF) of ϵ_{beam} within a beam ($|a| \leq a_{\text{out}}$) can be written as

$$\frac{d\psi(\epsilon_{\text{beam}})}{d \log_{10} \epsilon_{\text{beam}}} = \frac{2 \ln 10}{a_{\text{out}}^2} \epsilon_{\text{beam}} a(\epsilon_{\text{beam}}) \left| \frac{da}{d\epsilon_{\text{beam}}} \right|, \quad (5)$$

where $a(\epsilon_{\text{beam}})$ is the inverse function of Equation (4) in the range of $a > 0$. In the bottom panel of Figure 2, we show the PDF defined by Equation (5). We note that the PDF is not

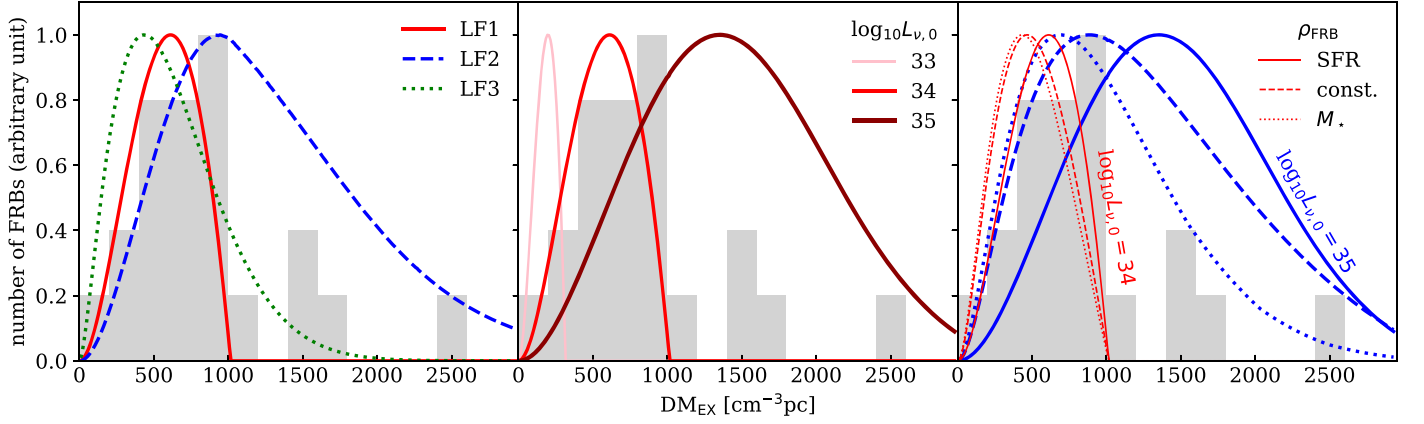


Figure 5. The DM_{IGM} distributions of detectable FRBs predicted with our models. LF1 with $\log_{10} L_{\nu,0}$ ($\text{erg s}^{-1} \text{Hz}^{-1}$) = 34, and the SFR model of ρ_{FRB} are used, unless otherwise stated. The DM distribution of the Parkes sample are shown together (gray histogram). Left panel: the predicted DM_{IGM} distributions with the three different LF models. Middle panel: the DM_{IGM} distributions with different $L_{\nu,0}$. Right panel: the DM_{IGM} distributions with the three different ρ_{FRB} models. Thin and thick lines indicate the distributions with $\log_{10} L_{\nu,0}$ ($\text{erg s}^{-1} \text{Hz}^{-1}$) = 34 and 35, respectively.

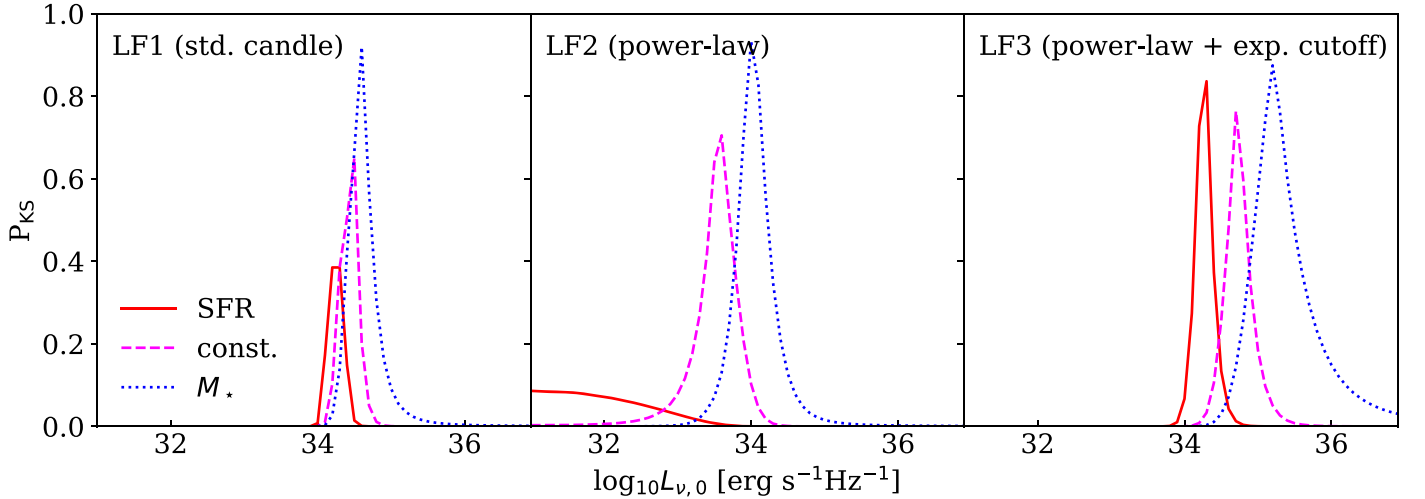


Figure 6. P_{KS} likelihood between the model and observed DM_{EX} distributions as a function of $L_{\nu,0}$. The left, middle, and right panels show P_{KS} for LF1, LF2, and LF3, respectively. The cases with the three ρ_{FRB} models are shown for each LF.

dependent on the choice of r_c , and is hence applicable to any radio telescope whose efficiency profile can be represented by an Airy disk.

3.2. Propagation Effects and K -correction

Flux density of an FRB is also affected by its propagation medium. While scattering may suppress FRB flux density by pulse broadening, scintillation and plasma lensing may also enhance FRB flux density (e.g., Hassall et al. 2013; Cordes et al. 2016, 2017). Currently, it is difficult to separate the intrinsic LF of FRBs from the PDF of the propagation effects. In this study, we consider effective luminosity ($L_{\nu,\text{eff}}$), which includes the propagation effects (ϵ_{prop}) rather than intrinsic luminosity ($L_{\nu,\text{int}}$) of an FRB. We also consider apparent luminosity ($L_{\nu,\text{app}}$) which includes ϵ_{beam} in addition to ϵ_{prop} and can be directly related to $S_{\nu,\text{app}}$.

K -correction is also an important effect when we consider observed flux densities of objects at cosmological distances.

We express the K -correction factor as

$$\kappa_{\nu}(z) = \frac{L_{\nu}(\nu_{\text{rest}})}{L_{\nu}(\nu_{\text{obs}})}, \quad (6)$$

where ν_{obs} is the observing frequency and $\nu_{\text{rest}} = (1+z)\nu_{\text{obs}}$. In the case of the Parkes multibeam receiver, $\nu_{\text{obs}} = 1.4 \text{ GHz}$. The functional form of $\kappa_{\nu}(z)$ is determined by spectra of FRBs, which are not yet known. Here we assume $\kappa_{\nu}(z) = 1$ (constant) and discuss how our results are affected by K -correction in Section 6.2.

In summary,

$$S_{\nu,\text{app}}(\nu_{\text{obs}}) = \frac{1+z}{4\pi d_L(z)^2} \kappa_{\nu}(z) L_{\nu,\text{app}}(\nu_{\text{obs}}), \text{ and} \quad (7)$$

$$L_{\nu,\text{app}}(\nu_{\text{obs}}) = \epsilon_{\text{beam}} L_{\nu,\text{eff}}(\nu_{\text{obs}}) \quad (8)$$

$$= \epsilon_{\text{beam}} \epsilon_{\text{prop}} L_{\nu,\text{int}}(\nu_{\text{obs}}), \quad (9)$$

where $d_L(z)$ is luminosity distance at redshift z .

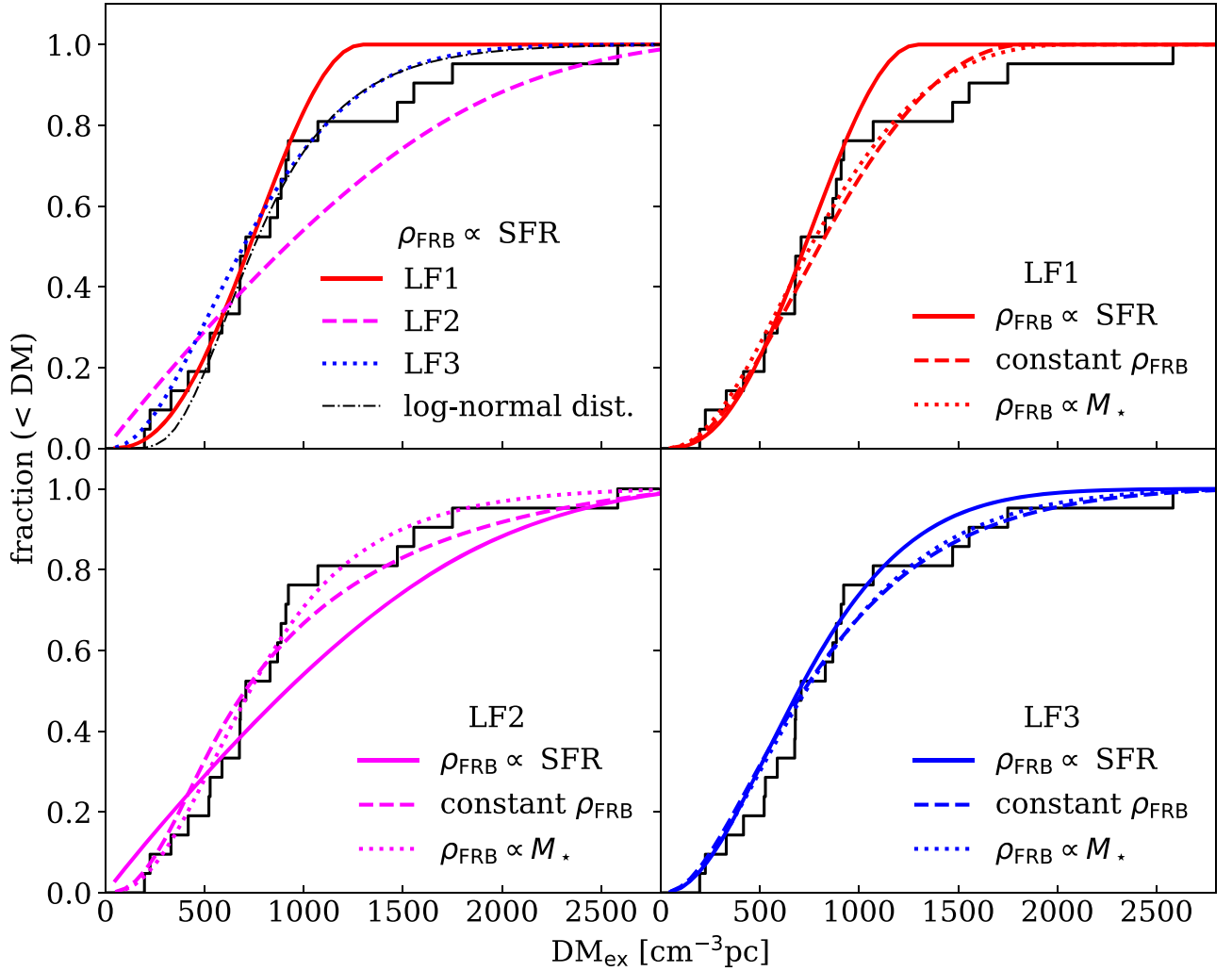


Figure 7. Cumulative DM_{EX} distribution of the Parkes FRB sample (histogram), and the best-fit model distributions to the observations. Top left panel: the best-fit models with LF1, LF2, and LF3 (solid (red), dashed (magenta), and dotted (blue) lines, respectively), the SFR model of ρ_{FRB} is assumed. A simple log-normal distribution with the median $DM_{\text{EX}} = 750 \text{ cm}^{-3} \text{ pc}$ and $\sigma = 0.2 \text{ dex}$ is plotted together (dotted-dashed line (black)). Top right, bottom left, and bottom right panels: the best-fit distributions with the different ρ_{FRB} models (SFR: solid line, constant: dashed line, and M_* : dotted line) with LF1, LF2, and LF3, respectively.

3.3. FRB LF

We examine the following three $L_{\nu, \text{eff}}$ distribution function models to demonstrate how difference of FRB LF affects the observable properties of FRBs.

1. LF1: FRBs are standard candles with $L_{\nu, \text{eff}} = L_{\nu, 0}$.
2. LF2: $L_{\nu, \text{eff}}$ follows a power-law distribution, $d\phi(L_{\nu, \text{eff}})/dL_{\nu, \text{eff}} \propto L_{\nu, \text{eff}}^{-2}$, with a faint-end cutoff at $L_{\nu, 0}$.
3. LF3: $L_{\nu, \text{eff}}$ follows a distribution function with the faint-end power-law index -1 down to $\log_{10} L_{\nu, \text{eff}} (\text{erg s}^{-1} \text{ Hz}^{-1}) = 30.0$, and exponential cutoff in the bright-end, $L_{\nu, \text{eff}} \gtrsim L_{\nu, 0}$, i.e., $d\phi(L_{\nu, \text{eff}})/dL_{\nu, \text{eff}} \propto x^{-1} \exp(-x)$, where $x = L_{\nu, \text{eff}}/L_{\nu, 0}$.

The three $L_{\nu, \text{eff}}$ PDFs and the corresponding $L_{\nu, \text{app}}$ PDFs are shown in Figure 3. The $L_{\nu, \text{app}}$ PDFs are obtained by convoluting the $L_{\nu, \text{eff}}$ PDFs with the ϵ_{beam} PDF (Equation (5)). The faint-end cutoff of LF3 is adopted so that the integral of the LF is finite. The cutoff luminosity can be observed at redshifts only up to $z \sim 0.01$ with the Parkes multibeam receiver, and hence it is faint enough not to affect our result.

Although the shape of the bright-end of the $L_{\nu, \text{app}}$ PDFs resembles that of the $L_{\nu, \text{eff}}$ PDFs, the faint-end of the $L_{\nu, \text{app}}$

PDFs is smeared out by the ϵ_{beam} variation. Hence it will be difficult to constrain the faint-end of the $L_{\nu, \text{eff}}$ PDFs from the currently observable properties of FRBs. Although the actual shape of the FRB LF is hardly known, we consider that the three LF models described above can represent a wide variety of LFs due to this smearing. We note that the PDF of ϵ_{prop} , and hence the $L_{\nu, \text{eff}}$ PDF, may depend on galactic latitude and longitude of observation fields, if the propagation effects in the Milky Way significantly affect observed flux densities. However, we assume that all FRBs under consideration arise from a single $L_{\nu, \text{eff}}$ PDF and consider the PDF to be the average of those in all observation fields.

3.4. Detection of an FRB

To constrain the FRB models, we use the sample of FRBs detected by the Parkes multibeam receiver before the end of 2017 November (21 FRBs between 010125 and 160102). The properties of the observed FRBs are taken from the FRBCAT¹ (Petroff et al. 2016). Although the values in the FRBCAT are

¹ <http://frbcat.org>

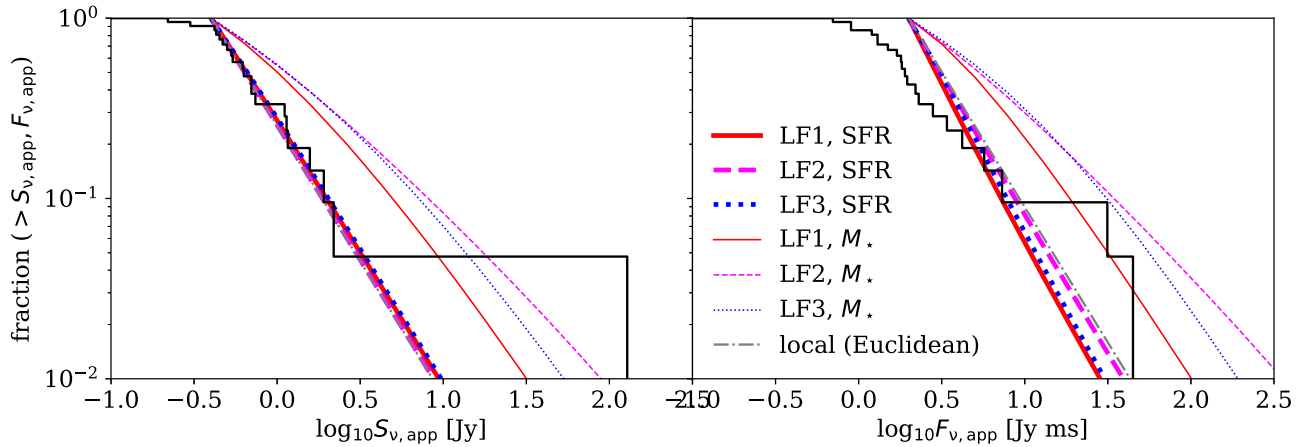


Figure 8. Left panel: the cumulative distribution of $S_{\nu, \text{app}}$ ($\log N - \log S$), predicted by the cosmological FRB models with the SFR and M_* models of ρ_{FRB} (thick and thin lines, respectively). The results with the three LF models are shown (LF1, LF2, and LF3; solid, dashed, and dotted lines, respectively). The $S_{\nu, \text{app}}$ distribution of the Parkes sample is plotted together (histogram), and the dotted–dashed line indicates the distribution in the Euclidean case ($\alpha = -1.5$). Right panel: same as the left panel but for $F_{\nu, \text{app}}$.

derived separately by individual authors, Petroff et al. (2016) have reanalyzed some of the data in a uniform manner, and we use the values derived by the reanalysis when available. We note that FRBs discovered by different telescopes should not be treated together in a statistical study of the DM distribution because the DM_{IGM} distribution of a sample of FRBs would depend on the detection limit of the observations.

We compute the fraction of detectable FRBs at each redshift using the $L_{\nu, \text{app}}$ distribution functions. For simplicity, we consider that an FRB is detected when the apparent flux density exceeds a threshold, $S_{\nu, \text{app}} \geq S_{\nu, \text{th}}$. To compare our model predictions with the Parkes detected FRB sample, we assume the threshold flux density $S_{\nu, \text{th}} = 0.4 \text{ Jy}$, which is comparable to the faintest FRBs in the Parkes sample.

Although it is pointed out that detectability of an FRB depends not only on its flux but also on the pulse width (and hence the fluence, Keane & Petroff 2015), the Parkes sample shows that $S_{\nu, \text{app}}$ is a better proxy for signal-to-noise ratio (S/N) than apparent fluence (observed fluence including ϵ_{beam} ($F_{\nu, \text{app}}$), see Figure 4). When the saturated event FRB 010724 (Lorimer et al. 2007) and the extremely bright outlier event FRB 150807 (Ravi et al. 2016) are excluded from the sample, the correlation coefficient between $\log_{10} S_{\nu, \text{app}}$ and $\log_{10} \text{S/N}$ is 0.79 (0.58 between $\log_{10} F_{\nu, \text{app}}$ and $\log_{10} \text{S/N}$). In Figure 5, we show how the predicted DM_{IGM} distribution of detectable FRBs depends on the assumed FRB models.

4. Luminosity of FRBs in the Case that They Originate at Cosmological Distances

Here we determine the characteristic luminosity density of FRBs ($L_{\nu, 0}$, see Section 3.3) that reproduces the observed DM_{EX} distribution best for each set of LF and ρ_{FRB} models, assuming that FRBs originate at cosmological distances and the observed DM_{EX} is dominated by DM_{IGM} . We evaluate the goodness of fit using the Kolmogorov–Smirnov (KS) test. Figure 6 shows the KS test probability (P_{KS}) that the observed sample can arise from the model distribution as a function of $L_{\nu, 0}$, and Figure 7 shows the best-fit DM_{IGM} distributions.

Although a wide variety of LF and ρ_{FRB} models agree with the observed DM_{EX} distribution, the model with $\rho_{\text{FRB}} \propto \text{SFR}$ plus LF2 does not reproduce the observations well. The best-fit $L_{\nu, 0}$ for the $\rho_{\text{FRB}} \propto \text{SFR}$ plus LF2 model is $\log_{10} L_{\nu, 0}$

($\text{erg s}^{-1} \text{ Hz}^{-1}$) ≤ 31 (P_{KS} is constant for smaller $L_{\nu, 0}$), which is smaller than the best-fit values for the other models. This is because LF2 makes the DM_{IGM} distribution heavily tailed in the high DM end, while the observed DM_{EX} distribution steeply declines above $\text{DM}_{\text{EX}} \gtrsim 1000 \text{ cm}^{-3} \text{ pc}$ (the left panel of Figure 5). The small $L_{\nu, 0}$ suppresses the high DM tail in the model distribution and minimizes the discrepancy between the model and observed distribution. However, it also overpredicts the number of FRBs with $\text{DM}_{\text{EX}} \lesssim 500 \text{ cm}^{-3} \text{ pc}$ making the model distribution broader than observed.

The discrepancy between the model with $\rho_{\text{FRB}} \propto \text{SFR}$ plus LF2 and the observations suggests that neither an FRB LF with an extended bright-end without cutoff, nor an FRB LF that is dominated by its faint-end is favorable to reproduce the observed narrow DM_{EX} distribution when $\rho_{\text{FRB}} \propto \text{SFR}$; though, the current FRB sample is not sufficient to rule out the model with high statistical significance. On the other hand, LF1 and LF3 reproduce the observations with similar $L_{\nu, 0}$ to each other ($\log_{10} L_{\nu, 0}$ ($\text{erg s}^{-1} \text{ Hz}^{-1}$) ~ 34 –35), indicating that the faint-end of a $L_{\nu, \text{eff}}$ PDF does not significantly affect the DM_{EX} distribution unless the $L_{\nu, \text{eff}}$ PDF is dominated by its faint-end as in the case of LF2 with $\log_{10} L_{\nu, 0}$ ($\text{erg s}^{-1} \text{ Hz}^{-1}$) $\lesssim 31$.

It is also noticeable that the $\rho_{\text{FRB}} \propto \text{SFR}$ plus LF1 model produce a sharp upper limit in the DM_{IGM} distribution that reflects the upper limit of the $L_{\nu, \text{eff}}$ distribution making the agreement between the model and the observations poorer than those with the other models, although it is not rejected with a certain statistical significance. The decrease in the number of FRBs above $\text{DM}_{\text{IGM}} \gtrsim 1000$ in the constant and M_* models (the bottom panel of Figure 1) can ease the conflict between LF1/LF2 and the observations. In those cases, LF2 also favors $\log_{10} L_{\nu, 0}$ ($\text{erg s}^{-1} \text{ Hz}^{-1}$) ~ 34 .

5. Are FRBs Cosmological or Local Events?

Although the cosmological DM_{IGM} models (except that with $\rho_{\text{FRB}} \propto \text{SFR}$ plus LF2) reproduce the observed DM_{EX} distribution well, as previously shown by Dolag et al. (2015), Katz (2016), and Caleb et al. (2016), it should be noted that the distribution can also be explained by a simple log-normal distribution with the median $\text{DM}_{\text{EX}} = 750 \text{ cm}^{-3} \text{ pc}$ and $\sigma = 0.2 \text{ dex}$ (shown in the top left panel of Figure 7). Since a log-normal distribution is one of the most commonly seen

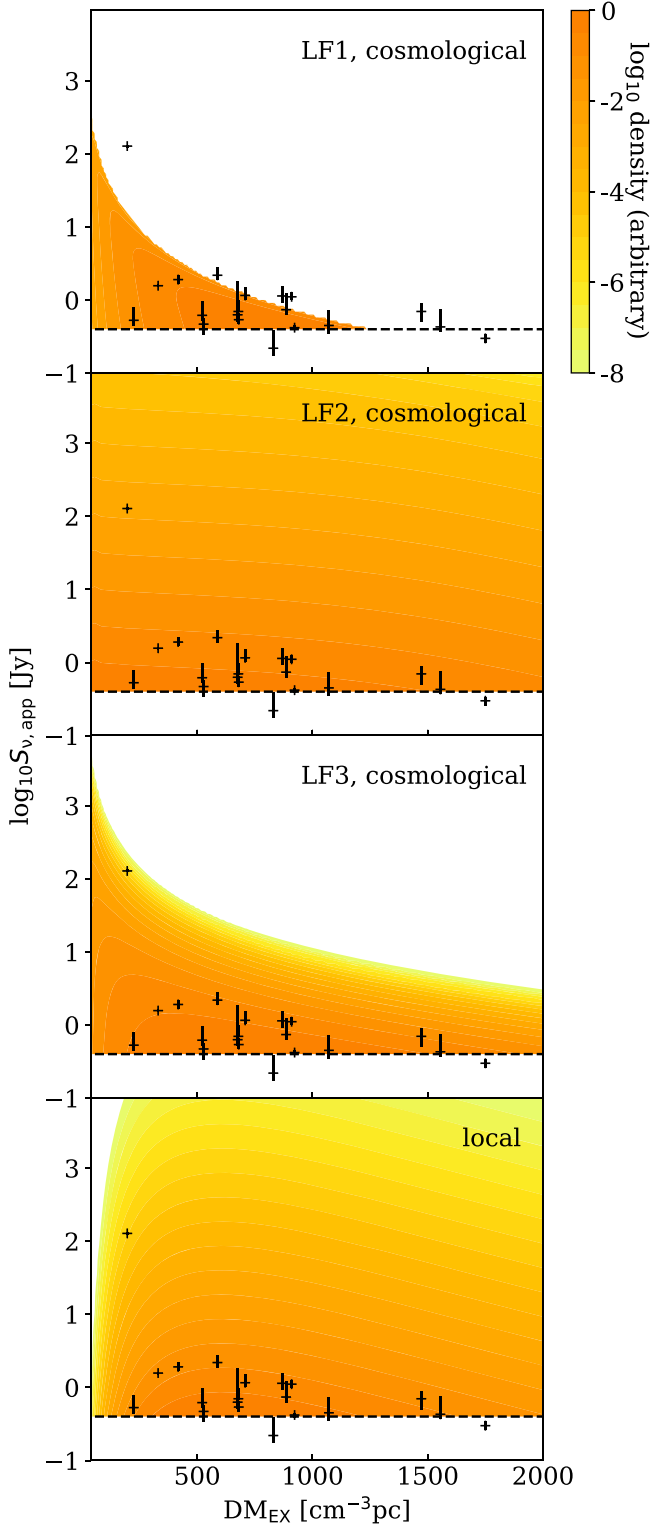


Figure 9. Distributions of FRBs on the parameter plane of DM_{EX} vs. $S_{\nu,\text{app}}$. The top three panels show the distributions of the cosmological FRBs with LF1, LF2, and LF3, respectively. ρ_{FRB} is assumed to be proportional to SFR. The bottom panel shows the distribution of the local FRB model. The horizontal dashed line indicates the assumed detection limit in our model (0.4 Jy). FRBs in the Parkes sample are overplotted with crosses.

PDFs in nature, it can be easily produced by a population of ionized gas in the circum/interstellar medium (CSM/ISM) around FRB sources without significant contribution from the IGM. Although a DM_{EX} as high as $750 \text{ cm}^{-3} \text{ pc}$ is not likely to

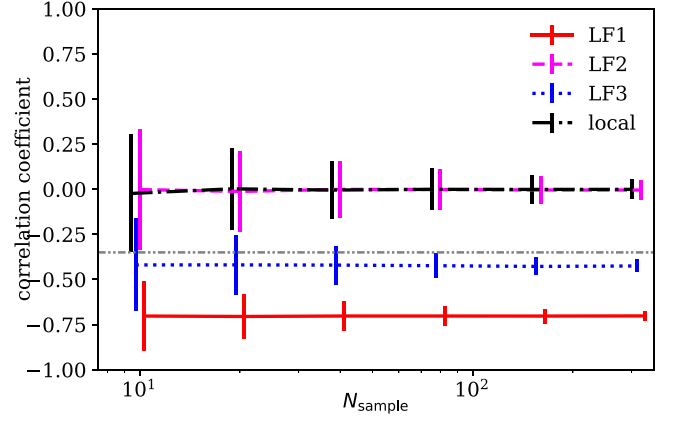


Figure 10. Mean and standard deviation of the correlation coefficient between DM_{EX} and $S_{\nu,\text{app}}$ generated by the Monte Carlo tests according to the distribution function shown in Figure 9. Data points connected with solid, dashed, and dotted lines show the correlation coefficient distribution with the cosmological FRB models with LF1, LF2, and LF3, respectively. The correlation coefficient distribution with the local FRB model is shown with data points connected with a dotted–dashed line. The data points are slightly shifted sideways for visibility. The horizontal double-dotted–dashed line indicates the correlation coefficient between DM_{EX} and $S_{\nu,\text{app}}$ in the Parkes sample with FRB 010724 and 150807 excluded ($N_{\text{sample}} = 19$). The random generation of mock sample is performed 1000 times for each N_{sample} .

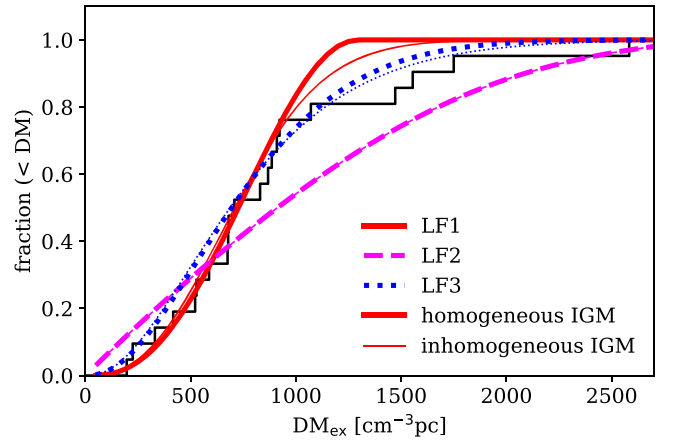


Figure 11. Cumulative DM_{EX} distributions predicted with (thin line) and without (thick line) the inhomogeneity of the IGM. The solid, dashed, and dotted lines represent the distributions predicted with LF1, LF2, and LF3, respectively. The SFR model of ρ_{FRB} is assumed. The distributions without the inhomogeneity are identical to those in Figure 7. DM_{EX} of the Parkes sample is plotted together (histogram).

arise from an ordinary galaxy ISM, if FRB sources are associated with ionized gas, such as a supernova remnant, it may significantly contribute to the observed DM_{EX} (Connor et al. 2016; Lyutikov et al. 2016; Murase et al. 2016; Piro 2016).

Here, we discuss how to distinguish whether FRBs are at cosmological distances (cosmological FRB model, DM_{EX} is dominated by DM_{IGM}) or in the local universe (local FRB model, DM_{EX} is dominated by CSM/ISM in the vicinity of FRB sources).

5.1. $\log N$ – $\log S$ Distribution

When a population of light sources is homogeneously distributed in a Euclidean space as in the case of the local FRB model, observed flux density and fluence of the sources (the so-

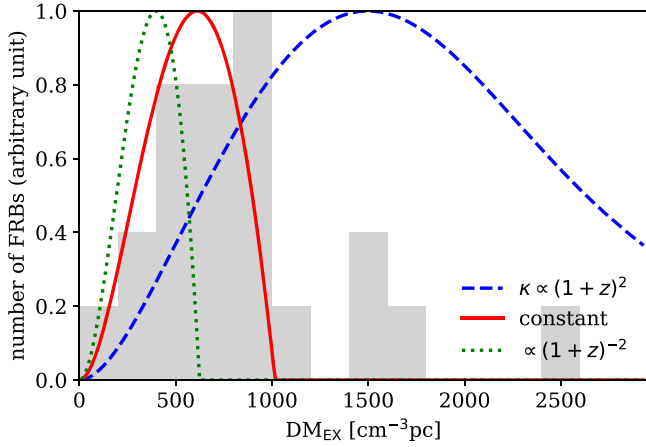


Figure 12. Same as Figure 5, but with $\beta = -2, 0$, and 2. LF1 with $\log_{10} L_{\nu,0}$ ($\text{erg s}^{-1} \text{Hz}^{-1}$) = 34, and the SFR model of ρ_{FRB} are assumed.

called $\log N$ – $\log S$ distribution) follow the power-law distribution $N(<S_\nu) \propto S_\nu^\alpha$ with index $\alpha = -1.5$. Although actual S_ν and F_ν of an FRB is not measurable due to the uncertain beam efficiency for each event, $S_{\nu,\text{app}}$ and $F_{\nu,\text{app}}$ would also follow the same power-law distribution when actual S_ν and F_ν follow the power-law distribution. Thus the observed distributions of $S_{\nu,\text{app}}$ and $F_{\nu,\text{app}}$ can serve as clues to distinguish whether FRBs are cosmological or local.

The earlier studies by Vedantham et al. (2016), Caleb et al. (2016), and Li et al. (2017) showed that the $F_{\nu,\text{app}}$ distribution is flatter than the Euclidean case ($\alpha > -1.5$). However, Macquart & Ekers (2018) pointed out that the $F_{\nu,\text{app}}$ distribution of FRBs are largely affected by the detection incompleteness in the faint-end, and the steepness of the distribution is dependent on the fluence limit applied in the analysis. The recent analyses by Macquart & Ekers (2018) and Bhandari et al. (2018) showed that the observed FRB sample indicates that the $F_{\nu,\text{app}}$ distribution is steeper than the Euclidean case ($\alpha < -1.5$) above the fluence completeness limit of 2 Jy ms (Keane & Petroff 2015), although the current FRB sample size is not sufficient to reject the Euclidean case. On the other hand, Oppermann et al. (2016) examined the distribution of S/Ns of FRBs rather than S_ν and F_ν , and found that the $\log N$ – $\log S$ distribution agrees well with the Euclidean case.

In the left panel of Figure 8, we show the predicted $S_{\nu,\text{app}}$ distributions by the cosmological FRB models assuming the SFR and M_\star models of ρ_{FRB} together with the three LF models. Hereafter, the parameter $L_{\nu,0}$ in the LF models is fixed to the best-fit value determined in Section 4, unless otherwise stated. The distribution functions predicted by the M_\star model of ρ_{FRB} are shallower than the Euclidean case regardless of the assumed LF model, while the distributions predicted by the SFR model of ρ_{FRB} are similar to the Euclidean case. This is because the cosmological expansion makes the $\log N$ – $\log S$ distribution shallower, while larger source density at larger distance (as in the case of the SFR model of ρ_{FRB}) makes the distribution steeper.

The right panel of Figure 8 shows the same distribution as that in the left panel but for $F_{\nu,\text{app}}$. We have assumed the PDF of FRB energy follow the same formulations as the LF (LF1, LF2, and LF3), with the characteristic energy $E_{\nu,0} = L_{\nu,0} \times 3 \text{ ms}$, and the fluence threshold of 2 Jy ms, which is the completeness limit derived by Keane & Petroff (2015); though, many FRBs are detected below this fluence.

The predicted $F_{\nu,\text{app}}$ distributions are steeper than the $S_{\nu,\text{app}}$ distributions because fluence is not affected by the cosmological expansion of time. As a result, the $F_{\nu,\text{app}}$ distribution functions predicted by the SFR model of ρ_{FRB} is steeper than the Euclidean case ($\alpha \sim -1.8$), being consistent with the suggestions by the recent observations (Bhandari et al. 2018; Macquart & Ekers 2018). Although the Euclidean case ($\alpha = -1.5$) is not fully ruled out by the current sample, if the steep fluence distribution is confirmed with the larger FRB sample, it indicates that FRBs originate at cosmological distances and ρ_{FRB} is larger at higher redshift resembling CSFH (see Section 6.2 for another possibility).

The difference of α between the $F_{\nu,\text{app}}$ distribution and the $S_{\nu,\text{app}}$ distribution predicted by the cosmological FRB models with $\rho_{\text{FRB}} \propto \text{SFR}$ can also reconcile the different α suggested by Oppermann et al. (2016, S/N distribution) and Macquart & Ekers (2018, $F_{\nu,\text{app}}$ distribution), given that $S_{\nu,\text{app}}$ correlates well with S/N. On the other hand, the shallow $\log N$ – $\log S$ distributions predicted by the M_\star model of ρ_{FRB} are close to the upper limit of α derived by Amiri et al. (2017), and hence can be rejected in the near future.

In the current Parkes sample, 9 out of the 21 FRBs have larger $F_{\nu,\text{app}}$ than the 2 Jy ms completeness limit. Macquart & Ekers (2018) examined how precisely α can be determined for a variation of FRB sample sizes. Their results suggest that ~ 50 FRBs above the fluence completeness limit would be necessary to distinguish $\alpha = -1.8$ (our model prediction) from the Euclidean case with a statistical significance of $\sim 95\%$. If the fraction of FRBs above the fluence completeness limit in the observed sample remains unchanged, the total sample size required will be ~ 100 FRBs.

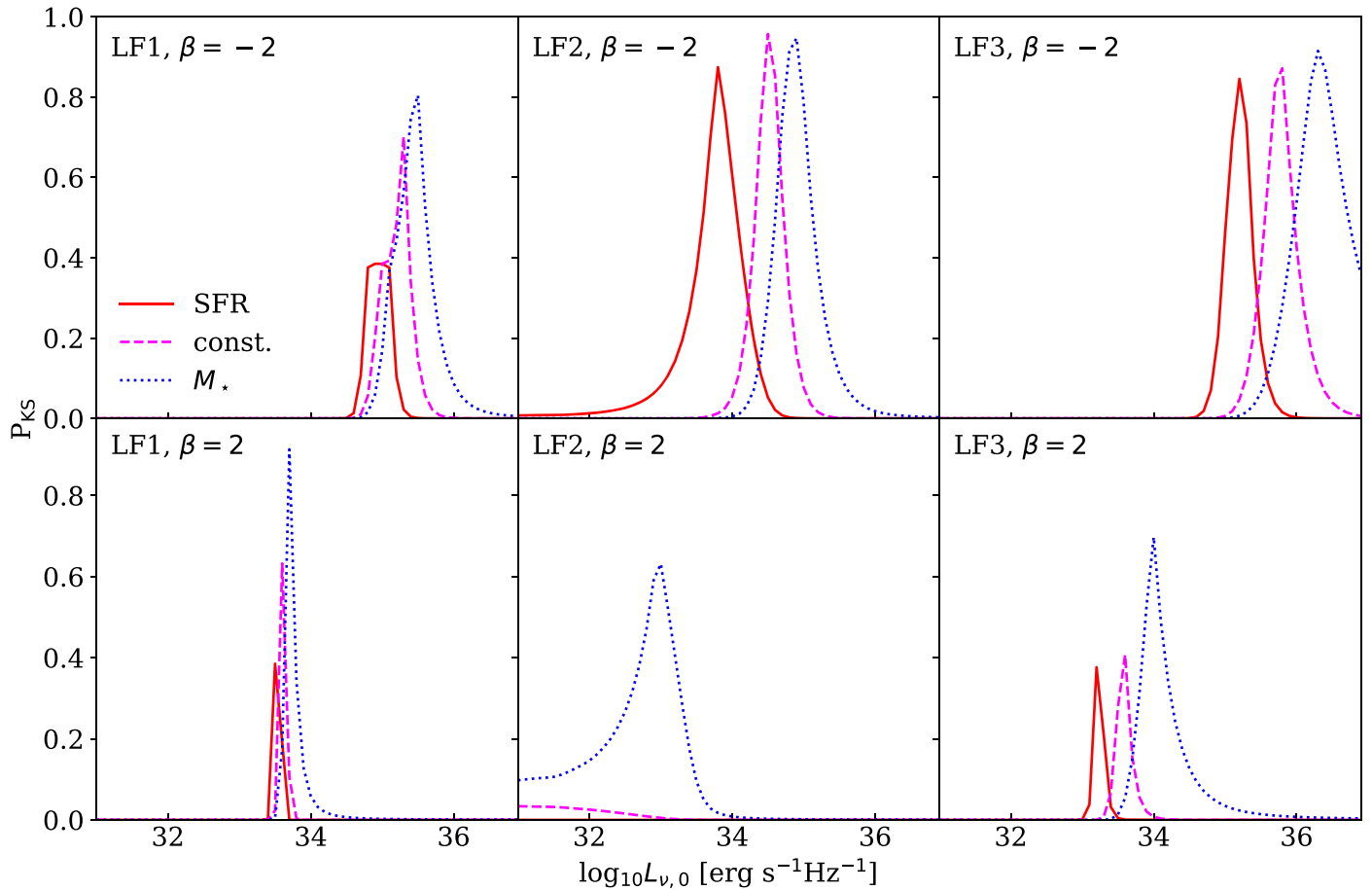
5.2. Correlation between DM_{EX} and $S_{\nu,\text{app}}$

Unlike $F_{\nu,\text{app}}$, $S_{\nu,\text{app}}$ correlates well with S/N and the cumulative distribution of $S_{\nu,\text{app}}$ does not show significant incompleteness in its faint end (Figures 4 and 8). Hence we might be able to utilize a larger observed sample when we investigate $S_{\nu,\text{app}}$ rather than $F_{\nu,\text{app}}$. However, the cumulative distribution of $S_{\nu,\text{app}}$ of the cosmological FRB model is similar to the Euclidean case (i.e., the local FRB model) when $\rho_{\text{FRB}} \propto \text{SFR}$, making it difficult to distinguish whether FRBs are cosmological or local solely with the $S_{\nu,\text{app}}$ distribution.

One possible clue is the correlation between DM_{EX} and $S_{\nu,\text{app}}$. Yang et al. (2017) investigated the correlation between DM_{EX} and observed flux density to constrain the contribution of CSM/ISM in the vicinity of FRBs to DM_{EX} but without taking account of the ϵ_{beam} variation within a receiver beam. Here we examine how efficiently the cosmological and local FRB models can be distinguished by the correlation between DM_{EX} and $S_{\nu,\text{app}}$ in the case of $\rho_{\text{FRB}} \propto \text{SFR}$.

We compute a distribution of FRBs on the parameter plane of DM_{EX} versus $S_{\nu,\text{app}}$ using the cosmological FRB models with LF1, LF2, and LF3 (the top three panels of Figure 9). For the local FRB model, we assume that the $\log N$ – $\log S$ distribution is the power law with $\alpha = -1.5$, and DM_{EX} follows the log-normal distribution with the median $DM_{\text{EX}} = 750 \text{ cm}^{-3} \text{ pc}$ and $\sigma = 0.2 \text{ dex}$ (the bottom panel of Figure 9).

We then randomly generate 10^3 sets of mock samples of DM_{EX} and $S_{\nu,\text{app}}$ with sample size N_{sample} each in accordance with the model distributions, and compute probability distribution of the correlation coefficient between DM_{EX} and $S_{\nu,\text{app}}$. In Figure 10, we show the mean and the standard deviation of the correlation coefficient distributions as functions of N_{sample} .

Figure 13. Same as Figure 6, but with $\beta = \pm 2$.

When the two peculiarly bright events, FRB 010724 and 150807, are excluded, the correlation coefficient between DM_{EX} and $S_{\nu, \text{app}}$ in the Parkes sample is -0.35 with $N_{\text{sample}} = 19$. The correlation coefficient in the Parkes sample is already outside the standard deviation of the local FRB model with the current N_{sample} . Although the correlation coefficient is still within the 2σ error of the local FRB model, it can be ruled out if the same correlation coefficient is obtained with $N_{\text{sample}} = 40$.

Among the cosmological FRB models with $\rho_{\text{FRB}} \propto \text{SFR}$, LF3 agrees best with the observations. The correlation coefficient distribution with LF2 is hardly distinguishable from that with the local FRB model; however, LF2 is disfavored by the DM_{EX} distribution (see Section 4). When the constant and M_* models of ρ_{FRB} are assumed, the correlation coefficient between DM_{EX} and $S_{\nu, \text{app}}$ is not significantly changed with LF1 and LF3, while the model with LF2 shows the correlation coefficient of approximately -0.2 to -0.3 depending on the ρ_{FRB} model.

If FRBs with higher DM_{EX} suffer more pulse broadening, it is possible that DM_{EX} and $S_{\nu, \text{app}}$ correlates even in the local FRB model because pulse broadening may decrease $S_{\nu, \text{app}}$. However, we note that the pulse width of the FRBs in the Parkes sample is not correlated with their DM_{EX} (the correlation coefficient is -0.003).

6. Discussion

6.1. Inhomogeneous IGM

In the previous sections, we have assumed that the IGM density is spatially uniform at each redshift. McQuinn (2014) computed a DM_{IGM} variation of FRBs at a single redshift caused

by the inhomogeneity of the IGM. Their results show that the standard deviation of DM_{IGM} is 20%–30% of the mean DM_{IGM} at each redshift in the range $z \sim 0.3$ – 1.4 when the spatial baryon distribution from a cosmological simulation is assumed.

To test how such DM_{IGM} variation affects the overall DM_{IGM} distribution that includes FRBs at various redshifts. We compute the DM_{IGM} distributions with the cosmological FRB models assuming that the probability distribution of $\log_{10} \text{DM}_{\text{IGM}}$ at a redshift follows a Gaussian distribution with the mean value determined by Equation (2) and $\sigma = 0.1$ dex. We find that the inhomogeneity of the IGM does not significantly affect either the overall DM_{IGM} distribution of FRBs, or the PDF of the correlation coefficient between DM_{EX} and $S_{\nu, \text{app}}$. The DM_{IGM} distributions predicted with and without the inhomogeneity of the IGM are shown in Figure 11.

6.2. K-correction

We have also assumed the K -correction factor to be $\kappa_\nu(z) = 1$ (constant). The real $\kappa_\nu(z)$ is determined by spectra of FRBs, which is not yet well known (see Equation (6)). For example, when the spectrum of an FRB is a power law, $L_{\nu, \text{eff}}(\nu) \propto \nu^\beta$, the K -correction factor is $\kappa_\nu(z) = (1+z)^\beta$. If $\kappa_\nu(z)$ increases with redshift, we would detect more FRBs at higher redshifts. In this sense, there is a degeneracy between the K -correction (spectrum) and ρ_{FRB} . In Figure 12, we show the DM_{IGM} distributions with $\beta = -2, 0$, and 2 , assuming LF1, $\rho_{\text{FRB}} \propto \text{SFR}$, and $\log_{10} L_{\nu, 0} \text{ (erg s}^{-1} \text{ Hz}^{-1}\text{)} = 34$.

We have determined the $L_{\nu,0}$ that reproduces the observed DM_{EX} distribution with $\beta = \pm 2$ following the same procedure as that in Section 4 (Figure 13). The observed DM_{EX} distribution can be reproduced in a wide variety of cases but with different $L_{\nu,0}$. Once the best-fit $L_{\nu,0}$ for each β is determined, the K -correction does not significantly affect the correlation coefficient between DM_{EX} and $S_{\nu,\text{app}}$. However, we note that $\beta > 0$ can also make the cumulative distribution of $F_{\nu,\text{app}}$ steeper as well as the increase of ρ_{FRB} at high redshifts, due to the degeneracy between the K -correction and ρ_{FRB} . Observations with different ν_{obs} are important to break the degeneracy.

7. Conclusions

We have computed the DM_{EX} distribution, the $\log N$ – $\log S$ distribution, and the DM_{EX} – $S_{\nu,\text{app}}$ correlation based on the analytic models of cosmic rate density history (ρ_{FRB}) and LF of FRBs. Comparing the model predictions with the observations, we have found that the cumulative distribution of apparent fluences suggests that FRBs are at cosmological distances with higher ρ_{FRB} at higher redshifts resembling CSFH (or FRBs typically have very hard radio spectra with L_{ν} larger at higher frequency, i.e., $\beta > 0$), although the sample size of the current observations is not sufficient to rule out that FRBs originate in the local universe.

If ρ_{FRB} is proportional to SFR, the narrow DM_{EX} distribution of the observed FRBs favors an FRB LF with a bright-end cutoff at $\log_{10} L_{\nu}$ ($\text{erg s}^{-1} \text{Hz}^{-1}$) ~ 34 . Although the constraint on the faint-end of FRB LF is rather weak, an FRB LF that is dominated by its faint-end is also disfavored. However, the statistical significance of the constraint with the current sample is still low.

The correlation coefficient between DM_{EX} and $S_{\nu,\text{app}}$ is potentially a very powerful tool to distinguish whether FRBs are at cosmological distances or in the local universe more robustly with future observations, which may provide us with higher statistical significance of the constraint than the $\log N$ – $\log S$ distribution for a given sample size.

We thank Yuan-Pei Yang and Liam D. Connor for their useful suggestions. Thanks are also due to the anonymous referee for encouraging comments. This research has been supported by JSPS KAKENHI grant No. JP17K14255.

ORCID iDs

Yuu Niino  <https://orcid.org/0000-0001-5322-5076>

References

- Amiri, M., Bandura, K., Berger, P., et al. 2017, *ApJ*, **844**, 161
 Bhandari, S., Keane, E. F., Barr, E. D., et al. 2018, *MNRAS*, **475**, 1427
 Caleb, M., Flynn, C., Bailes, M., et al. 2016, *MNRAS*, **458**, 708
 Cao, X.-F., Xiao, M., & Xiao, F. 2017, *RAA*, **17**, 14
 Chatterjee, S., Law, C. J., Wharton, R. S., et al. 2017, *Natur*, **541**, 58
 Connor, L., Sievers, J., & Pen, U.-L. 2016, *MNRAS*, **458**, L19
 Cordes, J. M., & Wasserman, I. 2016, *MNRAS*, **457**, 232
 Cordes, J. M., Wasserman, I., Hessels, J. W. T., et al. 2017, *ApJ*, **842**, 35
 Cordes, J. M., Wharton, R. S., Spitler, L. G., Chatterjee, S., & Wasserman, I. 2016, arXiv:1605.05890
 Dolag, K., Gaensler, B. M., Beck, A. M., & Beck, M. C. 2015, *MNRAS*, **451**, 4277
 Falcke, H., & Rezzolla, L. 2014, *A&A*, **562**, A137
 Fukugita, M., & Peebles, P. J. E. 2004, *ApJ*, **616**, 643
 Hassall, T. E., Keane, E. F., & Fender, R. P. 2013, *MNRAS*, **436**, 371
 Inoue, S. 2004, *MNRAS*, **348**, 999
 Ioka, K. 2003, *ApJL*, **598**, L79
 Kashiya, K., Ioka, K., & Mészáros, P. 2013, *ApJL*, **776**, L39
 Katz, J. I. 2016, *ApJ*, **818**, 19
 Keane, E. F., & Petroff, E. 2015, *MNRAS*, **447**, 2852
 Keane, E. F., Stappers, B. W., Kramer, M., & Lyne, A. G. 2012, *MNRAS*, **425**, L71
 Li, L.-B., Huang, Y.-F., Zhang, Z.-B., Li, D., & Li, B. 2017, *RAA*, **17**, 6
 Lorimer, D. R., Bailes, M., McLaughlin, M. A., Narkevic, D. J., & Crawford, F. 2007, *Sci*, **318**, 777
 Lyutikov, M., Burzawa, L., & Popov, S. B. 2016, *MNRAS*, **462**, 941
 Macquart, J.-P., & Ekers, R. D. 2018, *MNRAS*, **474**, 1900
 Madau, P., & Dickinson, M. 2014, *ARA&A*, **52**, 415
 McQuinn, M. 2014, *ApJL*, **780**, L33
 Murase, K., Kashiya, K., & Mészáros, P. 2016, *MNRAS*, **461**, 1498
 Oppermann, N., Connor, L. D., & Pen, U.-L. 2016, *MNRAS*, **461**, 984
 Palaniswamy, D., & Zhang, B. 2018, *ApJL*, **865**, L12
 Petroff, E., Barr, E. D., Jameson, A., et al. 2016, *PASA*, **33**, e045
 Piro, A. L. 2016, *ApJL*, **824**, L32
 Piro, A. L., & Burke-Spolaor, S. 2017, *ApJL*, **841**, L30
 Popov, S. B., & Postnov, K. A. 2013, arXiv:1307.4924
 Ravi, V., Shannon, R. M., Bailes, M., et al. 2016, *Sci*, **354**, 1249
 Staveley-Smith, L., Wilson, W. E., Bird, T. S., et al. 1996, *PASA*, **13**, 243
 Tendulkar, S. P., Bassa, C. G., Cordes, J. M., et al. 2017, *ApJL*, **834**, L7
 Thornton, D., Stappers, B., Bailes, M., et al. 2013, *Sci*, **341**, 53
 Totani, T. 2013, *PASJ*, **65**, L12
 Vedantham, H. K., Ravi, V., Hallinan, G., & Shannon, R. M. 2016, *ApJ*, **830**, 75
 Yang, Y.-P., Luo, R., Li, Z., & Zhang, B. 2017, *ApJL*, **839**, L25
 Zhang, B. 2017, *ApJL*, **836**, L32